Letter

Stacking-induced magnetic frustration and spiral spin liquid

Jianqiao Liu,[1,*] Xu-Ping Yao,[2,*] and Gang Chen[2,3,†]

[1]*State Key Laboratory of Surface Physics and Department of Physics, Fudan University, Shanghai 200433, China*

[2]*Department of Physics and HKU-UCAS Joint Institute for Theoretical and Computational Physics at Hong Kong, The University of Hong Kong, Hong Kong, China*

[3]*The University of Hong Kong Shenzhen Institute of Research and Innovation, Shenzhen 518057, China*

(Received 14 October 2022; revised 17 December 2022; accepted 20 December 2022; published 29 December 2022)

Like the twisting control in magic-angle twisted bilayer graphene, the stacking control is another mechanical approach to manipulate the fundamental properties of solids, especially the van der Waals materials. We explore the stacking-induced magnetic frustration and the spiral spin liquid on a multilayer triangular lattice antiferromagnet where the system is built from ABC stacking with competing intralayer and interlayers couplings. By combining the nematic bond theory and the self-consistent Gaussian approximation, we establish the phase diagram for this ABC-stacked multilayer magnet. It is shown that the system supports a wide regime of spiral spin liquid with multiple degenerate spiral lines in the reciprocal space, separating the low-temperature spiral order and the high-temperature featureless paramagnet. The transition to the spiral order from the spiral spin liquid regime is first order. We further show that the spiral-spin-liquid behavior persists even with small perturbations such as further neighbor intralayer exchanges. The connection to the ABC-stacked magnets, the effects of Ising or planar spin anisotropy, and the outlook on the stacking-engineered quantum magnets are discussed.

DOI: 10.1103/PhysRevB.106.L220410

Since the discovery of superconductivity [1], quantum anomalous Hall effect [2], and other phenomena [3–11] in twisted bilayer graphene, twistronics has emerged as an important and popular field in the study of two-dimensional (2D) materials. The crystal twisting provides an important control knob to manipulate the electronic properties of quantum materials and also to induce exotic quantum phases of matter in the underlying electronic systems. Like the more popular twisting scheme, the stacking control is another useful structural manipulation of the stacking orders of 2D materials through rotation and translation between the layers. The stacking procedure has been successfully used to manipulate the electronic and optical properties of layered van der Waals (vdW) materials [12–15], and the application to the 2D magnetism has recently been explored [16–18]. Modern fabrication techniques such as mechanical exfoliation [19–24] and molecular beam epitaxy [25,26] make such a stacking control of magnetism feasible. It was shown that the interlayer coupling depends strongly on the stacking, allowing the manipulation of the magnetic properties of the stacked magnets [16–18]. While existing works focus on the different magnetic orders resulting from the stacking, in this Letter we explore the possibility of stacking-induced magnetic frustration as well as liquidlike fluctuating regimes from frustration.

We start from the 2D magnet with the simplest frustrated structure, i.e., the triangular lattice, and stack the triangular layers along the c direction to form a multilayer three-dimensional (3D) system. The stacking order was known to be crucial in determining the electronic states [27–30]. For multilayer graphene, it was shown that different (chiral) stacking creates rather distinct low-energy descriptions for the electron bands [31–33], and thus leads to distinct and interesting electronic properties [12–14,34]. In the electronic systems, the stacking order changes the electronic properties by modifying the electron tunneling channels and the electron interactions. In magnets, the stacking order of the magnetic layers influences the lattice structure and then the magnetic interaction. Among many different possible stacking orders, we here choose an ABC stacking of the triangular layers. This choice turns out to be one of the simplest stackings that could generate magnetic frustration and nontrivial magnetic physics. Clearly, the AA stacking is a simple uniform stacking along the c direction and does not really lead to anything interesting if only the nearest-neighbor (NN) interaction is considered. The AB stacking, where the reference site of the B layer is projected to the center of the triangular plaquette on the A layer, generates interesting magnetic correlations and belongs to the extensively studied bipartite lattices. The ABC stacking in Fig. 1(a), that seemingly triples the crystal unit cell, is in fact a 3D Bravais lattice. By creating a corner-shared tetrahedral structure along the c axis, the ABC stacking drastically enhances the magnetic frustration and can induce a classical spin-liquid regime at low temperatures even for Ising spins [35]. Together with the intralayer interaction from the ABC-stacked structure, the interlayer interactions generate rich and interesting magnetic behaviors including the subextensive ground-state degeneracy, thermal order-by-disorder, magnetic transition to spiral orders, thermal crossover, and

*These authors contributed equally to this work.
†gangchen@hku.hk

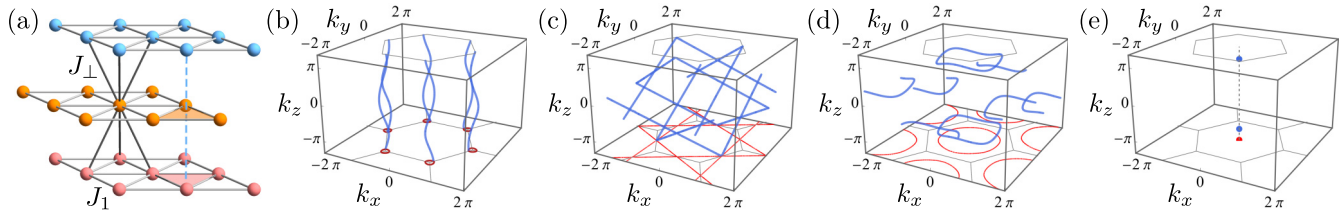

FIG. 1. (a) The multilayer triangular lattice with the ABC stacking. The dashed line along the c direction indicates the projection of a site from the top layer to the centers of unequivalent triangles within the lower two layers. The intralayer and interlayer interactions are denoted by J_1 and $J_\perp$, respectively. The spiral manifolds (blue) and their projections (red) on the k_x-k_y plane are presented for (b) $J_\perp/J_1 = 0.3$, (c) 1.0, (d) 1.5, and (e) 3.0. The BZ boundaries for a monolayer triangular lattice are plotted in gray.

spiral spin liquid (SSL) regimes. We reveal these behaviors with the intralayer and interlayer Heisenberg interactions using a set of analytical techniques.

For each site of the ABC-stacking triangular multilayers, there exist six NN sites within the same layer and three in each of the two adjacent layers. Distinct from the AB-stacking case, the triangular layer is no longer a mirror plane in the ABC-stacked case. Instead, the lattice site becomes an inversion center. The primitive lattice vectors are chosen as $\boldsymbol{a}_1 = (1, 0, 0)$, $\boldsymbol{a}_2 = (-1/2, \sqrt{3}/2, 0)$, $\boldsymbol{a}_3 = (1/2, \sqrt{3}/6, h)$, where the interlayer separation h varies for different materials. In this Letter, we take a unit layer distance $h = 1$ for convenience. Starting from the NN antiferromagnetic Heisenberg model on the triangular lattice, we incorporate the NN interlayer spin interactions with the Hamiltonian

$$\mathcal{H} = J_1 \sum_{\langle ij\rangle_\parallel} \mathbf{S}_i \cdot \mathbf{S}_j + J_\perp \sum_{\langle ij\rangle_\perp} \mathbf{S}_i \cdot \mathbf{S}_j. \tag{1}$$

Here $\langle ij\rangle_\parallel$ and $\langle ij\rangle_\perp$ refer to intra- and interlayer NN pairs, respectively. The antiferromagnetic interactions are denoted by J_1 and $J_\perp$ [see Fig. 1(a)]. In the decoupling limit where $J_\perp/J_1 = 0$, the ground state on the monolayer triangular lattice is the well-known 120° state. As we demonstrate below, the ABC stacking drastically enhances the magnetic frustration and suppresses the magnetic ordering once the interlayer coupling is considered.

I. ZERO-TEMPERATURE CLASSICAL GROUND STATES

By performing the Fourier transformation on the spin operator $\mathbf{S}_i = \frac{1}{\sqrt{N_s}} \sum_{\boldsymbol{k}} \mathbf{S}_{\boldsymbol{k}} e^{\imath \boldsymbol{k}\cdot\boldsymbol{r}_i}$, the spin Hamiltonian can be recast in the reciprocal space as $\mathcal{H} = \sum_{\boldsymbol{k}} \mathbf{S}_{-\boldsymbol{k}} \mathcal{J}(\boldsymbol{k}) \mathbf{S}_{\boldsymbol{k}}$, where N_s is the total number of spins, $\mathcal{J}(\boldsymbol{k}) = \sum_{\boldsymbol{d}_{ij}} J_{ij} e^{\imath \boldsymbol{k}\cdot\boldsymbol{d}_{ij}}$ is the exchange interaction, and $\boldsymbol{d}_{ij} \equiv \boldsymbol{r}_i - \boldsymbol{r}_j$ denotes the NN vectors for both intra- and interlayer bonds. Following the recipe of the Luttinger-Tisza method, this local unit-length constraint $|\mathbf{S}_i| = 1$ for each spin is softened and replaced by a global one $\sum_i |\mathbf{S}_i| = N_s$. The classical ground state of the spin Hamiltonian can be obtained by searching the minimum eigenvalues of $\mathcal{J}(\boldsymbol{k})$ and verifying the satisfaction of the local constraints. It is convenient to introduce a complex parameter $\xi(\boldsymbol{k}) \equiv \Lambda(\boldsymbol{k}) e^{\imath\theta(\boldsymbol{k})} = 1 + e^{\imath \boldsymbol{k}\cdot\boldsymbol{a}_1} + e^{\imath \boldsymbol{k}\cdot(\boldsymbol{a}_1+\boldsymbol{a}_2)}$, where its modulus and argument have been assigned to be $\Lambda(\boldsymbol{k})$ and $\theta(\boldsymbol{k})$, respectively. The exchange interaction is further rewritten as

$$\mathcal{J}(\boldsymbol{k}) = \tfrac{1}{2} J_1 [\Lambda(\boldsymbol{k})^2 - 3] + J_\perp \Lambda(\boldsymbol{k}) \cos[\boldsymbol{k}\cdot\boldsymbol{a}_3 - \theta(\boldsymbol{k})]. \tag{2}$$

At this stage, the minima of $\mathcal{J}(\boldsymbol{k})$ are simply characterized by $\xi(\boldsymbol{k}) = -e^{\imath \boldsymbol{k}\cdot\boldsymbol{a}_3} J_\perp/J_1$. By solving the equation about $\xi(\boldsymbol{k})$, the propagation vectors of the eigenvalue minima form several 1D manifolds in the reciprocal space for $0 < J_\perp/J_1 < 3$ as shown in Figs. 1(b)–1(d). In particular, a spin-spiral state can be constructed through these propagation vectors and satisfies the local constraints strictly. Therefore, the spiral manifolds with a subextensive degeneracy from the Luttinger-Tisza method are the physical ground states. They are responsible for the formation of the SSL of the $(d_s, d_c) = (1, 2)$ type [36,37] at finite temperatures when thermal fluctuations are introduced. Here d_s and d_c refer to the dimension and codimension of spiral manifolds, respectively.

The degenerate spiral manifold evolves with $J_\perp/J_1$. In the weak interlayer coupling regime where $J_\perp/J_1 < 1$, the spiral manifolds manifest as six helices in Fig. 1(b). Their projections onto the k_x-k_y plane are comprised of six disconnected contours around the K points in the Brillouin zone (BZ) for the monolayer triangular system. As $J_\perp/J_1$ increases from 0 to 1, the helices and their projected contours expands concurrently. For $J_\perp/J_1 = 1$, the spiral manifolds cross each other and become intersected lines in Fig. 1(c). The degeneracy of the ground states reaches its maximum as well and indicates the strongest magnetic frustration. In the strong interlayer coupling regime with $1 < J_\perp/J_1 < 3$, the degenerate spiral manifold is further reduced into discrete and distort contours as shown in Fig. 1(d). Their contours decrease with increasing $J_\perp/J_1$. Finally, they shrink into the points at $(0, 0, \pm\pi)$ when $J_\perp/J_1 \geqslant 3$. The ground state turns out to be the antiferromagnetic (ferromagnetic) order between (within) the triangular layers.

II. THERMAL ORDER BY DISORDER

As the temperature increases from absolute zero, the thermal fluctuations enter into the system and could lift the subextensive ground-state degeneracy. For weak thermal fluctuations at low temperatures, this induces a discrepancy in the entropy for the spin-spiral wave vector on the spiral manifold, despite the fact that different spin spiral configurations share the same energy. The one that possesses the highest entropy would be stabilized. This mechanism for the establishment of the long-range orders is known as the thermal order-by-disorder [36,38–40]. To formulate this effect for our case, we perform the low-temperature free energy and entropy calculation, and the details can be found in the Supplemental Material (SM) [41]. In Fig. 2(a), we further depict the phase diagram

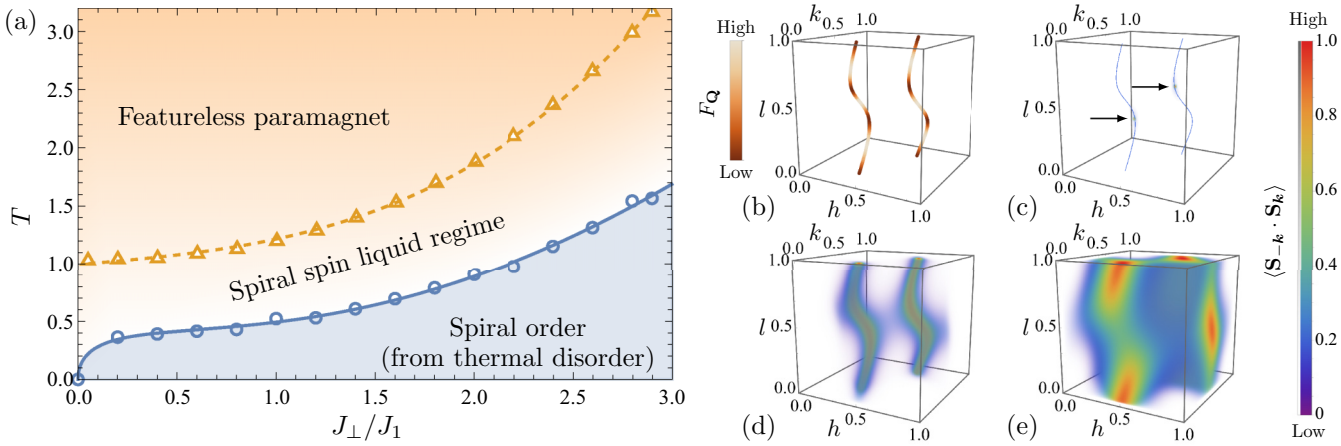

FIG. 2. (a) The classical phase diagram for the J_1-$J_\perp$ Heisenberg model on an ABC-stacked triangular lattice. The crossover (first-order phase transition) is outlined by the dashed (solid) line. (b) The distribution of free energy $F_\mathbf{Q}$ on the spiral manifolds for $J_\perp/J_1 = 0.5$. The NBT results of $\langle \mathbf{S}_{-k} \cdot \mathbf{S}_k \rangle$ in (c) the spiral ordered phase with $T = 0.229$, (d) the SSL regime with $T = 0.429$, and (e) the high-temperature paramagnet with $T = 1.589$. The regions with the lower density are set to be more transparent. The arrows in (b) indicate the positions where $\langle \mathbf{S}_{-k} \cdot \mathbf{S}_k \rangle$ are highly concentrated on the spiral manifolds (blue). The system size is $50 \times 50 \times 50$.

and mark the regimes of thermal order by disorder. The finite temperature SSL regime is discussed in the later part of the Letter.

We sketch the thermal order-by-disorder effect here. At low temperatures, the thermal fluctuations of the spins are around the ground-state manifold. To characterize the thermal fluctuation of the spins, it is more convenient to parameterize the fluctuating spins based on the spin configurations from the ground-state manifold. For an arbitrary spin-spiral order with wave vector $\mathbf{Q}$, the spins would deviate from their ordered orientations $\bar{\mathbf{S}}_i = [\cos(\mathbf{Q} \cdot \boldsymbol{r}_i), \sin(\mathbf{Q} \cdot \boldsymbol{r}_i), 0]$ due to the thermal fluctuations. This deviation can be described by a perpendicular vector $\boldsymbol{\phi}_i$ as $\mathbf{S}_i = \boldsymbol{\phi}_i + \bar{\mathbf{S}}_i(1 - \phi_i^2)^{1/2}$, and $|\phi_i| \ll 1$ at very low temperatures. To capture the low-temperature properties, it is sufficient to expand the Hamiltonian up to the quadratic order of the in-plane and out-of-plane components ϕ_i^{i} and ϕ_i^{o} with $\mathcal{H}_\phi = \sum_{ij} \tilde{J}_{ij} \phi_i^{\mathrm{o}} \phi_j^{\mathrm{o}} + \tilde{J}_{ij} (\bar{\mathbf{S}}_i \cdot \bar{\mathbf{S}}_j) \phi_i^{\mathrm{i}} \phi_j^{\mathrm{i}}$ and $\tilde{J}_{ij} = J_{ij} - \delta_{ij} \mathcal{J}(\mathbf{Q})$. Under this approximation, the low-temperature free energy is given by

$$F_\mathbf{Q} \sim T \int_{\boldsymbol{k}} \ln W_\mathbf{Q}(\boldsymbol{k}) + C, \tag{3}$$

where $W_\mathbf{Q}(\boldsymbol{k}) = -\mathcal{J}(\mathbf{Q}) + \sum_{\boldsymbol{d}_{ij}} J_{ij} e^{\imath \boldsymbol{k} \cdot \boldsymbol{d}_{ij}} \cos(\mathbf{Q} \cdot \boldsymbol{d}_{ij})$ and C is a constant. In Fig. 2(b), we plot the distribution of $\mathbf{Q}$-dependent free energy $F_\mathbf{Q}$ on the spiral manifolds for $J_\perp/J_1 = 0.5$. The relative strength of $F_\mathbf{Q}$ is encoded into the color gradient, and the darkest points represent the selected wave vectors whose exact coordinates have been listed in the SM [41].

III. THE FINITE-TEMPERATURE BEHAVIORS

Upon further increasing the temperatures, the selected spin spiral orders via the thermal order by disorder would melt under the strong thermal fluctuations. Before entering into a featureless paramagnet, the SSL could be revived at intermediate temperatures. To fully reveal the finite-temperature behaviors, we here implement a nematic bond theory (NBT) [42] and the conventional self-consistent Gaussian approximation (SCGA) to construct the classical phase diagram, which has been shown in Fig. 2(a). Both methods start from the partition function in the form of an imaginary-time functional integral

$$\mathcal{Z} = \int \mathcal{D}[\mathbf{S}] \mathcal{D}[\chi] \, e^{-\beta \mathcal{H}} \, e^{-\imath \beta \sum_i \chi_i (|\mathbf{S}_i|^2 - 1)}, \tag{4}$$

where the Lagrange multiplier χ_i serves as an auxiliary field to impose the local constraint and β is the inverse of temperature.

In the NBT framework, the auxiliary constraint field $\chi_{k-k'}$ is divided into the static sector $\Delta(T) = \imath \chi_{k=0}$ and the fluctuating sector $\mathrm{X}_{k,k'} = -\imath \chi_{k-k'}(1 - \delta_{k,k'})$ after the Fourier transformation. The separation of variables yields the action

$$\mathcal{S} = \beta \sum_{k,k'} \mathbf{S}_{-k} (K_{k,k'} - \mathrm{X}_{k,k'}) \cdot \mathbf{S}_{k'} - \beta V \Delta(T), \tag{5}$$

where $K_{k,k'} \equiv K_{0,k} \delta_{k,k'} = [\mathcal{J}(\boldsymbol{k}) + \Delta(T)] \delta_{k,k'}$. An effective partition function $\mathcal{Z} = \int d\Delta \, e^{\beta V \Delta(T)} \mathcal{Z}[\Delta]$ can be obtained after the integration over the spin components in the large-N limit [41]. The effective action in $\mathcal{Z}[\Delta]$ is in the power of the field X. To integrate the fluctuating sector X out, the self-consistent equations should be established for the bare spin propagators $\langle \mathbf{S}_{-k} \cdot \mathbf{S}_k \rangle = (2\beta)^{-1} N K_{0,k}^{-1}$ and the inverse constraint field propagators $\langle \chi_{-k} \, \chi_k \rangle^{-1} = D_{0,k}^{-1} = N/2 \sum_{k'} K_{0,k+k'}^{-1} K_{0,k'}^{-1}$. They are renormalized perturbatively by the higher order X terms in $\mathcal{Z}[\Delta]$ and thus dressed by the a proper self-energy Σ and polarization Π, respectively. The resulting Dyson equations are

$$K_{\mathrm{eff},k} = K_{0,k} - \Sigma_k, \tag{6}$$

$$D_{\mathrm{eff},k}^{-1} = D_{0,k}^{-1} - \Pi_k. \tag{7}$$

As suggested in Ref. [42], at the cost of omitting all vertex corrections, the Dyson equations can be solved self-consistently

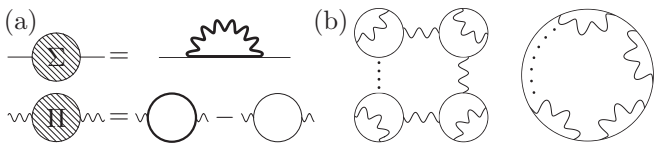

FIG. 3. (a) Self-consistent equations for the self-energy Σ and polarization Π. (b) The derivative loop diagrams in the free-energy density.

with

$$\Sigma_{\boldsymbol{k}} = -\sum_{\boldsymbol{k}'\neq 0} K^{-1}_{\mathrm{eff},\boldsymbol{k}-\boldsymbol{k}'} D_{\mathrm{eff},\boldsymbol{k}'}, \tag{8}$$

$$\Pi_{\boldsymbol{k}} = D^{-1}_{0,\boldsymbol{k}} - \frac{N}{2}\sum_{\boldsymbol{k}'} K^{-1}_{\mathrm{eff},\boldsymbol{k}+\boldsymbol{k}'} K^{-1}_{\mathrm{eff},\boldsymbol{k}'}, \tag{9}$$

and are depicted as the diagrams in Fig. 3(a). With these approximations, the final integral in $\mathcal{Z}$ over the static sector Δ can be evaluated at the saddle point where $NT/(2V)\sum_{\boldsymbol{k}} K^{-1}_{\mathrm{eff},\boldsymbol{k}} = 1$. The free-energy density, that includes the loop diagrams in Fig. 3(b), are derived explicitly [41].

For the concerned parameter regime $0 < J_\perp/J_1 < 3$ where there exists a subextensive degeneracy, the concentrated weights of spin structure factors $\langle \mathbf{S}_{-\boldsymbol{k}} \cdot \mathbf{S}_{\boldsymbol{k}} \rangle$, that are calculated with the NBT, are found in the low-temperature regime at the discrete momentum points, indicating the spin-spiral orders. As shown in Fig. 2(c), the positions of these high weights are identical to the results based on the entropy and the thermal order-by-disorder calculations. Moreover, the free-energy density manifests a first-order phase transition above the ordered states at the temperatures shown in Fig. 2(a). The distribution of $\langle \mathbf{S}_{-\boldsymbol{k}} \cdot \mathbf{S}_{\boldsymbol{k}} \rangle$ also changes drastically. Right above the transition temperature T_C, the pointlike concentrations of $\langle \mathbf{S}_{-\boldsymbol{k}} \cdot \mathbf{S}_{\boldsymbol{k}} \rangle$ disappear immediately. Instead, there are clear spectral weight enhancements around the spiral manifold, and they decay rapidly away from it as shown in Fig. 2(d). These features are characteristic to the SSL [36,37] and persist within a broad temperature window [see Fig. 2(a)].

The SSL behaviors are gradually overwhelmed with the prevailing thermal fluctuations. At higher temperatures, the spectral weights of $\langle \mathbf{S}_{-\boldsymbol{k}} \cdot \mathbf{S}_{\boldsymbol{k}} \rangle$ tend to spread throughout the whole BZ as shown in Fig. 2(e). Eventually, the spectral peaks around the spiral manifolds would become indiscernible when the system is deeply in the featureless paramagnet. The system experiences a crossover from the SSL to the featureless paramagnet. In the description of the NBT, the fluctuating sector $\mathrm{X}_{\boldsymbol{k},\boldsymbol{k}'}$ of the constraint field becomes insignificant and can be neglected in Eq. (5). This simplification in the NBT leads to the well-known SCGA, which can qualitatively describe this thermal crossover [41]. In the phase diagram of Fig. 2(a), the crossover temperatures are outlined based on the "smoothening" of the spectral peaks [41]. Physically, this thermal crossover from higher temperatures to lower temperatures corresponds to the growth of the spin correlation. At a temperature much above Curie temperature, all the spins are fluctuating thermally and there is not much correlation between the spins. At the order of the Curie temperature, the spins become gradually correlated. At even lower temperatures in the SSL regime, the spin correlation in the momentum space reveals the structures of the degenerate spiral manifold. In the SSL regime, the thermal fluctuations are mainly around the spiral manifold, which may resemble the thermal fluctuation near a critical point to some extent, and a semiuniversal thermodynamic property is expected. It is found that the specific heat behaves like $C_V = c_1 + c_2 T$ in the SSL regime, where $c_{1,2}$ are constants [41].

IV. SUBLEADING SPIN INTERACTIONS

While the thermal order-by-disorder and the entropy effect could lift the degeneracy of the spiral manifold at low temperatures, it is well-known that other subleading spin interactions could enter and break the degeneracy. For instance, in the presence of the second- and third-nearest spin interactions (denoted as J_2 and J_3, respectively), the spiral manifolds only exist at a special point $J_2/J_1 = 2J_3/J_1$ and $0 < J_\perp/J_1 \leqslant 3 + 30J_3/J_1$ [41]. While this effect is clearly important at low temperatures, especially in the relevant $\mathrm{AC_rO_2}$ antiferromagnets [50], the more tempting question is about the stability of the SSL regime that is connected to the degenerate spiral manifold. Or, more experimentally, can the degenerate spiral manifold still manifest itself in the finite-temperature spin correlation? Certainly, when the subleading interaction is rather weak, this is expected. To what extent the spin correlation is modified by the subleading interaction, however, depends on the several competing energy scales and could vary from material to material. It is, therefore, more appropriate to simply demonstrate this for the specific interactions that are relevant to certain materials. We have performed the NBT calculations for $(J_1, J_2, J_3, J_\perp) = (1.0, 0.0, 0.13, 0.1)$ that are closely relevant to the first-principles results for α-$\mathrm{HC_rO_2}$ [50]. The spin-spiral orders at low-temperatures are confirmed through the magnetic Bragg peak of $\langle \mathbf{S}_{-\boldsymbol{k}} \cdot \mathbf{S}_{\boldsymbol{k}} \rangle$ [see Fig. 4(a)]. A first-order transition is evidenced at $T_C \approx 0.470$ [41].

The spectral weights of $\langle \mathbf{S}_{-\boldsymbol{k}} \cdot \mathbf{S}_{\boldsymbol{k}} \rangle$ become pronounced along the degenerate spiral manifolds once the temperature exceeds T_C. Its specific thermal evolution, however, carries a bit more structure. Within a narrow window $T_C < T \lesssim 0.573$, the most prominent weights appear near the ordered wave vectors [indicated by arrows in Fig. 4(b)]. With increasing temperature, two consecutive crossovers can be identified. First, the inhomogeneity of $\langle \mathbf{S}_{-\boldsymbol{k}} \cdot \mathbf{S}_{\boldsymbol{k}} \rangle$ along the degenerate spiral manifold is quickly flattened with the growing thermal fluctuations. A more homogeneous distribution is recovered when $T \gtrsim 0.573$, as shown in Fig. 4(c). Finally, the system undergoes another crossover into the featureless paramagnet, as indicated by the spreading of $\langle \mathbf{S}_{-\boldsymbol{k}} \cdot \mathbf{S}_{\boldsymbol{k}} \rangle$ in Fig. 4(d).

V. DISCUSSION

The J_1-$J_\perp$ Heisenberg model for the SSL physics is quite distinct from previous studies based on bipartite lattices [37,51]. Due to the geometric frustrations that are naturally induced by the ABC stacking, an *infinitesimal* interlayer coupling is sufficient to spawn the SSL. For bipartite lattice models, a finite interaction threshold is required for the SSL.

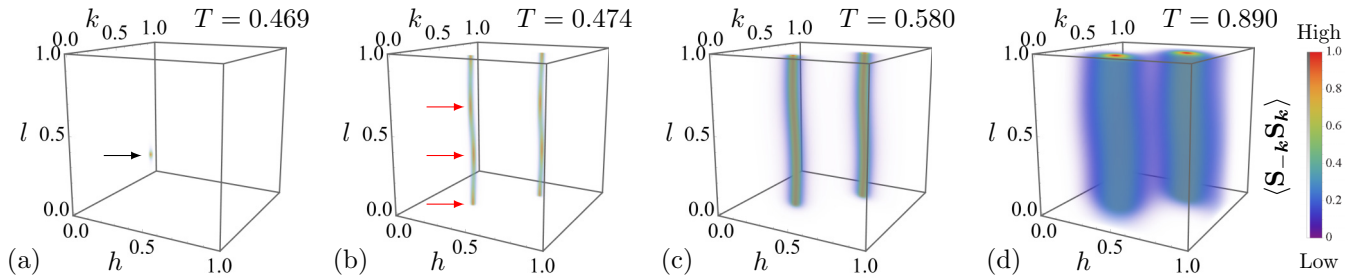

FIG. 4. The NBT results of $\langle \mathbf{S}_{-\boldsymbol{k}} \cdot \mathbf{S}_{\boldsymbol{k}} \rangle$ at $(J_1, J_\perp, J_2, J_3) = (1.0, 0.1, 0.0, 0.13)$ for the system size $50 \times 50 \times 50$. The first two temperatures are very close to the first-order transition temperature $T_C \approx 0.470$. The arrows indicate the (a) pointlike and (b) arc-shape concentrations of $\langle \mathbf{S}_{-\boldsymbol{k}} \cdot \mathbf{S}_{\boldsymbol{k}} \rangle$, respectively.

For example, the criteria are $J_2/J_1 > 1/6$ for the honeycomb lattice [52], $J_2/J_1 > 1/8$ for the diamond lattice [36], and more strictly $J_2/J_1 = 2J_3/J_1 > 1/4$ for the square lattice [51]. This restriction may challenge the realization of SSLs because further exchange interactions can be relatively weak in real materials. The SSL condition $0 < J_\perp/J_1 < 3$ for our model is immediately realized once the stacking structure is fabricated to a sufficient number of layers.

Even for few layers, the SSL physics is still expected. When descending to a bilayer, our model is equivalent to a J_1-J_2 Heisenberg model on a honeycomb lattice. Furthermore, for even numbers of layers, the ABC-stacked triangular lattice can be viewed as a multilayer honeycomb lattice still with the ABC stacking despite a displacement of two sublattices along the c direction. Very recently, a 2D SSL has been advocated by neutron scattering measurements in a vdW honeycomb magnet $FeCl_3$ with the same stacking [53]. It is also immune to intricate interlayer couplings. Although the interlayer spin exchanges are different here, a similar SSL is promising, e.g., through appropriate stacking controls. The nature of a few-layer version of our model is worthy of further study.

Besides the stacking fabrication of vdW materials, ABC-stacked triangular multilayer magnets actually exist in nature. There are a family of magnets with the formula AMX_2 where A is a monovalent metal, M is a trivalent metal such as the transition metal ion Cr [50,54–57] or the rare-earth ion [58–61], and X is a chalcogen, and the rhombohedral vdW compounds MX_2 such as $NiBr_2$ and NiI_2 [62–66]. Both families of magnets could experience extra magnetic anisotropies beyond the simple Heisenberg model. The simplest and common anisotropy for the transition metal ions such as Cr^{3+} and Ni^{2+} ions is the single-ion spin anisotropy. In the presence of the easy-plane anisotropy, it is still possible to construct the spiral orders within the XY plane, and the SSL physics is still expected. With the easy-axis spin anisotropy, one cannot construct spiral orders with Ising spins and thus the ground-state configurations are completely different. The thermal fluctuations, however, could violate the Ising constraint and induce the SSL regime [45,47]. Besides the characteristics as shown in Figs. 2(c)–2(e), the spin structure factors could possess a reciprocal kagomé-like structure from the competition between frustration and spin stiffness [47]. The magnetic anisotropy for the rare-earth chalcogenides AMX_2 is mainly the exchange anisotropy from the strong spin-orbit coupling. Because of the short-range orbitals of the $4f$ electrons, the spin exchange is most likely to be dominated by the intralayer interactions, and the SSL physics due to the interlayer coupling is probably less relevant over there. The mechanical control such as twisting, bending, and stacking is an uprising control knob of the physical properties of quantum materials. We hope our work to stimulate some interest in the stacking control of quantum magnets and materials.

ACKNOWLEDGMENTS

We thank Chun-Jiong Huang for useful discussions. This work is supported by the National Science Foundation of China with Grant No. 92065203, the Ministry of Science and Technology of China with Grant No. 2021YFA1400300, by the Shanghai Municipal Science and Technology Major Project with Grant No. 2019SHZDZX01, by NNSF of China with Grant No. 12174067, and by the Research Grants Council of Hong Kong with General Research Fund Grant No. 17306520.

[1] Y. Cao, V. Fatemi, S. Fang, K. Watanabe, T. Taniguchi, E. Kaxiras, and P. Jarillo-Herrero, Unconventional superconductivity in magic-angle graphene superlattices, Nature (London) **556**, 43 (2018).

[2] M. Serlin, C. L. Tschirhart, H. Polshyn, Y. Zhang, J. Zhu, K. Watanabe, T. Taniguchi, L. Balents, and A. F. Young, Intrinsic quantized anomalous Hall effect in a moiré heterostructure, Science **367**, 900 (2020).

[3] Y. Cao, V. Fatemi, A. Demir, S. Fang, S. L. Tomarken, J. Y. Luo, J. D. Sanchez-Yamagishi, K. Watanabe, T. Taniguchi, E. Kaxiras, R. C. Ashoori, and P. Jarillo-Herrero, Correlated insulator behaviour at half-filling in magic-angle graphene superlattices, Nature (London) **556**, 80 (2018).

[4] M. Yankowitz, S. Chen, H. Polshyn, Y. Zhang, K. Watanabe, T. Taniguchi, D. Graf, A. F. Young, and C. R. Dean, Tuning superconductivity in twisted bilayer graphene, Science **363**, 1059 (2019).

[5] A. L. Sharpe, E. J. Fox, A. W. Barnard, J. Finney, K. Watanabe, T. Taniguchi, M. A. Kastner, and D. Goldhaber-

Gordon, Emergent ferromagnetism near three-quarters filling in twisted bilayer graphene, Science **365**, 605 (2019).

[6] D. Wong, K. P. Nuckolls, M. Oh, B. Lian, Y. Xie, S. Jeon, K. Watanabe, T. Taniguchi, B. A. Bernevig, and A. Yazdani, Cascade of electronic transitions in magic-angle twisted bilayer graphene, Nature (London) **582**, 198 (2020).

[7] K. P. Nuckolls, M. Oh, D. Wong, B. Lian, K. Watanabe, T. Taniguchi, B. A. Bernevig, and A. Yazdani, Strongly correlated Chern insulators in magic-angle twisted bilayer graphene, Nature (London) **588**, 610 (2020).

[8] Y. Choi, H. Kim, Y. Peng, A. Thomson, C. Lewandowski, R. Polski, Y. Zhang, H. S. Arora, K. Watanabe, T. Taniguchi, J. Alicea, and S. Nadj-Perge, Correlation-driven topological phases in magic-angle twisted bilayer graphene, Nature (London) **589**, 536 (2021).

[9] Y. Saito, F. Yang, J. Ge, X. Liu, T. Taniguchi, K. Watanabe, J. I. A. Li, E. Berg, and A. F. Young, Isospin Pomeranchuk effect in twisted bilayer graphene, Nature (London) **592**, 220 (2021).

[10] N. C. H. Hesp, I. Torre, D. Rodan-Legrain, P. Novelli, Y. Cao, S. Carr, S. Fang, P. Stepanov, D. Barcons-Ruiz, H. Herzig Sheinfux, K. Watanabe, T. Taniguchi, D. K. Efetov, E. Kaxiras, P. Jarillo-Herrero, M. Polini, and F. H. L. Koppens, Observation of interband collective excitations in twisted bilayer graphene, Nat. Phys. **17**, 1162 (2021).

[11] Y. Xie, A. T. Pierce, J. M. Park, D. E. Parker, E. Khalaf, P. Ledwith, Y. Cao, S. H. Lee, S. Chen, P. R. Forrester, K. Watanabe, T. Taniguchi, A. Vishwanath, P. Jarillo-Herrero, and A. Yacoby, Fractional Chern insulators in magic-angle twisted bilayer graphene, Nature (London) **600**, 439 (2021).

[12] W. Bao Jr, L. Jing, J. Velasco, Y. Lee, G. Liu, D. Tran, B. Standley, M. Aykol, S. B. Cronin, D. Smirnov, M. Koshino, E. McCann, M. Bockrath, and C. N. Lau, Stacking-dependent band gap and quantum transport in trilayer graphene, Nat. Phys. **7**, 948 (2011).

[13] C. H. Lui, Z. Li, K. F. Mak, E. Cappelluti, and T. F. Heinz, Observation of an electrically tunable band gap in trilayer graphene, Nat. Phys. **7**, 944 (2011).

[14] Y. Shan, Y. Li, D. Huang, Q. Tong, W. Yao, W.-T. Liu, and S. Wu, Stacking symmetry governed second harmonic generation in graphene trilayers, Sci. Adv. **4**, eaat0074 (2018).

[15] T. Jiang, H. Liu, D. Huang, S. Zhang, Y. Li, X. Gong, Y.-R. Shen, W.-T. Liu, and S. Wu, Valley and band structure engineering of folded MoS_2 bilayers, Nat. Nanotechnol. **9**, 825 (2014).

[16] W. Chen, Z. Sun, Z. Wang, L. Gu, X. Xu, S. Wu, and C. Gao, Direct observation of van der Waals stacking-dependent interlayer magnetism, Science **366**, 983 (2019).

[17] T. Li, S. Jiang, N. Sivadas, Z. Wang, Y. Xu, D. Weber, J. E. Goldberger, K. Watanabe, T. Taniguchi, C. J. Fennie, K. Fai Mak, and J. Shan, Pressure-controlled interlayer magnetism in atomically thin CrI_3, Nat. Mater. **18**, 1303 (2019).

[18] T. Song, Z. Fei, M. Yankowitz, Z. Lin, Q. Jiang, K. Hwangbo, Q. Zhang, B. Sun, T. Taniguchi, K. Watanabe, M. A. McGuire, D. Graf, T. Cao, J.-H. Chu, D. H. Cobden, C. R. Dean, D. Xiao, and X. Xu, Switching 2D magnetic states via pressure tuning of layer stacking, Nat. Mater. **18**, 1298 (2019).

[19] B. Huang, G. Clark, E. Navarro-Moratalla, D. R. Klein, R. Cheng, K. L. Seyler, D. Zhong, E. Schmidgall, M. A. McGuire, D. H. Cobden, W. Yao, D. Xiao, P. Jarillo-Herrero, and X. Xu, Layer-dependent ferromagnetism in a van der Waals crystal down to the monolayer limit, Nature (London) **546**, 270 (2017).

[20] C. Gong, L. Li, Z. Li, H. Ji, A. Stern, Y. Xia, T. Cao, W. Bao, C. Wang, Y. Wang, Z. Q. Qiu, R. J. Cava, S. G. Louie, J. Xia, and X. Zhang, Discovery of intrinsic ferromagnetism in two-dimensional van der Waals crystals, Nature (London) **546**, 265 (2017).

[21] Z. Fei, B. Huang, P. Malinowski, W. Wang, T. Song, J. Sanchez, W. Yao, D. Xiao, X. Zhu, A. F. May, W. Wu, D. H. Cobden, J.-H. Chu, and X. Xu, Two-dimensional itinerant ferromagnetism in atomically thin Fe_3GeTe_2, Nat. Mater. **17**, 778 (2018).

[22] Y. Deng, Y. Yu, Y. Song, J. Zhang, N. Z. Wang, Z. Sun, Y. Yi, Y. Z. Wu, S. Wu, J. Zhu, J. Wang, X. H. Chen, and Y. Zhang, Gate-tunable room-temperature ferromagnetism in two-dimensional Fe_3GeTe_2, Nature (London) **563**, 94 (2018).

[23] J.-U. Lee, S. Lee, J. H. Ryoo, S. Kang, T. Y. Kim, P. Kim, C.-H. Park, J.-G. Park, and H. Cheong, Ising-type magnetic ordering in atomically thin $FePS_3$, Nano Lett. **16**, 7433 (2016).

[24] X. Wang, K. Du, Y. Y. F. Liu, P. Hu, J. Zhang, Q. Zhang, M. H. S. Owen, X. Lu, C. K. Gan, P. Sengupta, C. Kloc, and Q. Xiong, Raman spectroscopy of atomically thin two-dimensional magnetic iron phosphorus trisulfide ($FePS_3$) crystals, 2D Mater. **3**, 031009 (2016).

[25] D. J. O'Hara, T. Zhu, A. H. Trout, A. S. Ahmed, Y. K. Luo, C. H. Lee, M. R. Brenner, S. Rajan, J. A. Gupta, D. W. McComb, and R. K. Kawakami, Room temperature intrinsic ferromagnetism in epitaxial manganese selenide films in the monolayer limit, Nano Lett. **18**, 3125 (2018).

[26] M. Bonilla, S. Kolekar, Y. Ma, H. C. Diaz, V. Kalappattil, R. Das, T. Eggers, H. R. Gutierrez, M.-H. Phan, and M. Batzill, Strong room-temperature ferromagnetism in VSe_2 monolayers on van der Waals substrates, Nat. Nanotechnol. **13**, 289 (2018).

[27] K. F. Mak, J. Shan, and T. F. Heinz, Electronic Structure of Few-Layer Graphene: Experimental Demonstration of Strong Dependence on Stacking Sequence, Phys. Rev. Lett. **104**, 176404 (2010).

[28] N. Sivadas, S. Okamoto, X. Xu, C. J. Fennie, and D. Xiao, Stacking-dependent magnetism in bilayer CrI_3, Nano Lett. **18**, 7658 (2018).

[29] P. Jiang, C. Wang, D. Chen, Z. Zhong, Z. Yuan, Z.-Y. Lu, and W. Ji, Stacking tunable interlayer magnetism in bilayer CrI_3, Phys. Rev. B **99**, 144401 (2019).

[30] Z. Wu, K. Bu, W. Zhang, Y. Fei, Y. Zheng, J. Gao, X. Luo, Z. Liu, Y.-P. Sun, and Y. Yin, Effect of stacking order on the electronic state of $1T-TaS_2$, Phys. Rev. B **105**, 035109 (2022).

[31] A. H. Castro Neto, F. Guinea, N. M. R. Peres, K. S. Novoselov, and A. K. Geim, The electronic properties of graphene, Rev. Mod. Phys. **81**, 109 (2009).

[32] H. Min and A. H. MacDonald, Electronic structure of multilayer graphene, Prog. Theor. Phys. Suppl. **176**, 227 (2008).

[33] C. Bao, W. Yao, E. Wang, C. Chen, J. Avila, M. C. Asensio, and S. Zhou, Stacking-dependent electronic structure of trilayer graphene resolved by nanospot angle-resolved photoemission spectroscopy, Nano Lett. **17**, 1564 (2017).

[34] S. H. Jhang, M. F. Craciun, S. Schmidmeier, S. Tokumitsu, S. Russo, M. Yamamoto, Y. Skourski, J. Wosnitza, S. Tarucha, J. Eroms, and C. Strunk, Stacking-order dependent transport properties of trilayer graphene, Phys. Rev. B **84**, 161408(R) (2011).

[35] D. T. Liu, F. J. Burnell, L. D. C. Jaubert, and J. T. Chalker, Classical spin liquids in stacked triangular-lattice Ising antiferromagnets, Phys. Rev. B **94**, 224413 (2016).

[36] D. Bergman, J. Alicea, E. Gull, S. Trebst, and L. Balents, Order-by-disorder and spiral spin-liquid in frustrated diamond-lattice antiferromagnets, Nat. Phys. **3**, 487 (2007).

[37] X.-P. Yao, J. Q. Liu, C.-J. Huang, X. Wang, and G. Chen, Generic spiral spin liquids, Front. Phys. **16**, 53303 (2021).

[38] J. Villain, R. Bidaux, J.-P. Carton, and R. Conte, Order as an effect of disorder, J. Phys. France **41**, 1263 (1980).

[39] C. L. Henley, Ordering Due to Disorder in a Frustrated Vector Antiferromagnet, Phys. Rev. Lett. **62**, 2056 (1989).

[40] J. N. Reimers and A. J. Berlinsky, Order by disorder in the classical Heisenberg kagomé antiferromagnet, Phys. Rev. B **48**, 9539 (1993).

[41] See Supplemental Material at http://link.aps.org/supplemental/10.1103/PhysRevB.106.L220410 for detailed information, which includes Refs. [35–37,42–49].

[42] M. Schecter, O. F. Syljuåsen, and J. Paaske, Nematic Bond Theory of Heisenberg Helimagnets, Phys. Rev. Lett. **119**, 157202 (2017).

[43] O. F. Syljuåsen, J. Paaske, and M. Schecter, Interplay between magnetic and vestigial nematic orders in the layered J_1–J_2 classical Heisenberg model, Phys. Rev. B **99**, 174404 (2019).

[44] C. Glittum and O. F. Syljuåsen, Arc-shaped structure factor in the J_1–J_2–J_3 classical Heisenberg model on the triangular lattice, Phys. Rev. B **104**, 184427 (2021).

[45] F. J. Burnell and J. T. Chalker, Frustration and correlations in stacked triangular-lattice Ising antiferromagnets, Phys. Rev. B **92**, 220417(R) (2015).

[46] S. V. Isakov, K. Gregor, R. Moessner, and S. L. Sondhi, Dipolar Spin Correlations in Classical Pyrochlore Magnets, Phys. Rev. Lett. **93**, 167204 (2004).

[47] C.-J. Huang, J. Q. Liu, and G. Chen, Spiral spin liquid behavior and persistent reciprocal kagome structure in frustrated van der Waals magnets and beyond, Phys. Rev. Res. **4**, 013121 (2022).

[48] H. T. Diep and H. Kawamura, First-order phase transition in the fcc Heisenberg antiferromagnet, Phys. Rev. B **40**, 7019 (1989).

[49] M. V. Gvozdikova and M. E. Zhitomirsky, A Monte Carlo study of the first-order transition in a Heisenberg FCC antiferromagnet, J. Exp. Theor. Phys. Lett. **81**, 236 (2005).

[50] K. Somesh, Y. Furukawa, G. Simutis, F. Bert, M. Prinz-Zwick, N. Büttgen, A. Zorko, A. A. Tsirlin, P. Mendels, and R. Nath, Universal fluctuating regime in triangular chromate antiferromagnets, Phys. Rev. B **104**, 104422 (2021).

[51] N. Niggemann, M. Hering, and J. Reuther, Classical spiral spin liquids as a possible route to quantum spin liquids, J. Phys.: Condens. Matter **32**, 024001 (2020).

[52] A. Mulder, R. Ganesh, L. Capriotti, and A. Paramekanti, Spiral order by disorder and lattice nematic order in a frustrated Heisenberg antiferromagnet on the honeycomb lattice, Phys. Rev. B **81**, 214419 (2010).

[53] S. Gao, M. A. McGuire, Y. Liu, D. L. Abernathy, C. d. Cruz, M. Frontzek, M. B. Stone, and A. D. Christianson, Spiral Spin Liquid on a Honeycomb Lattice, Phys. Rev. Lett. **128**, 227201 (2022).

[54] A. Olariu, P. Mendels, F. Bert, B. G. Ueland, P. Schiffer, R. F. Berger, and R. J. Cava, Unconventional Dynamics in Triangular Heisenberg Antiferromagnet $NaCrO_2$, Phys. Rev. Lett. **97**, 167203 (2006).

[55] J. Liu, B. Liu, L. Yuan, B. Li, L. Xie, X. Chen, H. Zhang, D. Xu, W. Tong, J. Wang, and Y. Li, Frustrated magnetism of the triangular-lattice antiferromagnets α-CrOOH and α-CrOOD, New J. Phys. **23**, 033040 (2021).

[56] F. Xiao, T. Lancaster, P. J. Baker, F. L. Pratt, S. J. Blundell, J. S. Möller, N. Z. Ali, and M. Jansen, Magnetic transition and spin dynamics in the triangular Heisenberg antiferromagnet α-$KCrO_2$, Phys. Rev. B **88**, 180401(R) (2013).

[57] J. Huang, B. Shi, F. Pan, J. Wang, J. Liu, D. Xu, H. Zhang, T. Xia, and P. Cheng, Anisotropic magnetic properties and tunable conductivity in two-dimensional layered $NaCrX_2$ (X = Te,Se,S) single crystals, Phys. Rev. Mater. **6**, 094013 (2022).

[58] W. Liu, Z. Zhang, J. Ji, Y. Liu, J. Li, X. Wang, H. Lei, G. Chen, and Q. Zhang, Rare-earth chalcogenides: A large family of triangular lattice spin liquid candidates, Chin. Phys. Lett. **35**, 117501 (2018).

[59] M. M. Bordelon, E. Kenney, C. Liu, T. Hogan, L. Posthuma, M. Kavand, Y. Lyu, M. Sherwin, N. P. Butch, C. Brown, M. J. Graf, L. Balents, and S. D. Wilson, Field-tunable quantum disordered ground state in the triangular-lattice antiferromagnet $NaYbO_2$, Nat. Phys. **15**, 1058 (2019).

[60] P.-L. Dai, G. Zhang, Y. Xie, C. Duan, Y. Gao, Z. Zhu, E. Feng, Z. Tao, C.-L. Huang, H. Cao, A. Podlesnyak, G. E. Granroth, M. S. Everett, J. C. Neuefeind, D. Voneshen, S. Wang, G. Tan, E. Morosan, X. Wang, H.-Q. Lin *et al.*, Spinon Fermi Surface Spin Liquid in a Triangular Lattice Antiferromagnet $NaYbSe_2$, Phys. Rev. X **11**, 021044 (2021).

[61] M. M. Bordelon, C. Liu, L. Posthuma, P. M. Sarte, N. P. Butch, D. M. Pajerowski, A. Banerjee, L. Balents, and S. D. Wilson, Spin excitations in the frustrated triangular lattice antiferromagnet $NaYbO_2$, Phys. Rev. B **101**, 224427 (2020).

[62] Y. Tokunaga, D. Okuyama, T. Kurumaji, T. Arima, H. Nakao, Y. Murakami, Y. Taguchi, and Y. Tokura, Multiferroicity in $NiBr_2$ with long-wavelength cycloidal spin structure on a triangular lattice, Phys. Rev. B **84**, 060406(R) (2011).

[63] T. Kurumaji, S. Seki, S. Ishiwata, H. Murakawa, Y. Kaneko, and Y. Tokura, Magnetoelectric responses induced by domain rearrangement and spin structural change in triangular-lattice helimagnets NiI_2 and CoI_2, Phys. Rev. B **87**, 014429 (2013).

[64] Y. Tokura, S. Seki, and N. Nagaosa, Multiferroics of spin origin, Rep. Prog. Phys. **77**, 076501 (2014).

[65] K. F. Mak, J. Shan, and D. C. Ralph, Probing and controlling magnetic states in 2D layered magnetic materials, Nat. Rev. Phys. **1**, 646 (2019).

[66] A. S. Botana and M. R. Norman, Electronic structure and magnetism of transition metal dihalides: Bulk to monolayer, Phys. Rev. Mater. **3**, 044001 (2019).